Facile synthesis of mesoporous lithium titanate spheres for high rate lithium-ion batteries

Yu-Sheng Lin, Jenq-Gong Duh*

Department of Materials Science and Engineering, National Tsing Hua University, Hsinchu, Taiwan

ABSTRACT

Lithium titanate is synthesized from titanium isopropoxide and lithium acetate solution under hydrothermal environment and calcinations. Introducing acidized carbon black during synthesis can produce mesoporous $Li_4Ti_5O_{12}$. The crystalline structure and morphological observation of the as-synthesized mesoporous $Li_4Ti_5O_{12}$ are characterized by X-ray diffraction (XRD) and scanning electron microscopy, respectively. The mesoporous structure can be directly observed through BEI images of the cross-section sample. Besides, N_2 adsorption/desorption isotherm also displays a hysteresis loop, implying the beneficial evidence of mesoporous structure. The pore size distribution of mesoporous lithium titanate evaluated by BJH model is narrow, and the average size of voids is around 4 nm. It is demonstrated that the electrochemical performance is significantly improved by the mesoporous structure. The mesoporous lithium titanate exhibits a stable capacity of 140 mAhg^{-1} at 0.5 C. Besides, the reversible capacity at 30 C remains over half of that at 0.5 C. The superior *C*-rate performance is associated with the mesoporous structure, facilitating lithium transportation ability during cycling.

© 2011 Elsevier B.V. All rights reserved.

1. Introduction

In recent years, lithium-ion batteries (LIBs) have been used for electric vehicles (EVs) and hybrid electric vehicles (HEVs) to save oil and to decrease exhaust emissions. The increasing demand for higher energy density and power density of batteries in electronic devices has attracted investigators to develop new materials for lithium-ion batteries. In commercial lithium-ion batteries, carbonaceous materials are generally used as anode materials [1]. However, the theoretical capacity of graphite was only 372 mAhg^{-1}. Consequently, Sn-based and Si-based materials were used as the negative electrodes, due to higher theoretical capacity, higher lithium packing density and proper operating voltage [2]. Nevertheless, the most critical problem in Sn-based and Si-based materials was the severe volume change during cycling, limiting the cycle life of the cell and further reducing the possibility of commercialization [3,4].

Therefore, spinel lithium titanate $Li_4Ti_5O_{12}$, which is so-called zero-strain insertion material, has aroused researcher's attention recently, due to its potential application as anode material in high rate lithium batteries [5]. Spinel host has an excellent structure stability and a very small volume change during cycling. The space group of the spinel $Li_4Ti_5O_{12}$ is *Fd3m*. One part of lithium-ions are located at (8a) sites, the other part of lithium ions and all titanium ions at (16d) sites, and oxygen ions at (32e) sites [6]. During cycling, three moles of lithium ions in tetrahedral sites (8a) are capable of inserting into the octahedral sites (16c) of $Li_4Ti_5O_{12}$ lattices, forming $Li_7Ti_5O_{12}$ rocksalt structure [5,7]. It accommodates Li-ions to have a theoretical capacity of 175 mAhg^{-1} with excellent cyclability and displays a discharge platform approximating 1.55 V vs. Li/Li$^+$, which can avoid the reduction of organic electrolyte, thus reducing the impedance of cell and making batteries more safe.

On the other hand, $Li_4Ti_5O_{12}$ is a poor electrical conductor with a conductivity of only 10^{-13} S cm^{-1} at room temperature [8]. New strategy is to design porous or hollow structure of anode materials [9–17]. First, the local pores could accommodate the volume change during cycling, delaying capacity fading. Porous or hollow structure was also used in Sn-based and Si-based anode material [9,10]. Second, the pores could provide extra space for the storage of lithium ions, benefiting for enhancing specific capacity. Consequently, porous or hollow structure could reveal excellent *C*-rate performance. However, large pore size might cause instability of electrodes during rolling and reduction in energy density of cell, e.g. three dimensionally ordered macroporous structure or hollow structure [17]. Yet, small pore size might impede electrolyte from flowing in the electrodes, deteriorating the cycling performance. Accordingly, mesoporous $Li_4Ti_5O_{12}$ structures give an ideal host material for the rapid intercalation and deintercalation of lithium ions upon cycling and provide the possibility for efficient transport of electrons at the rapid lithium transportation [11,12]. Thus,

---

* Corresponding author. Tel.: +886 3 5712686; fax: +886 3 5712686.
E-mail address: jgd@mx.nthu.edu.tw (J.-G. Duh).

mesoporous structure of lithium titanate is indeed a superior material selection for lithium-ion batteries. The present work aims to improve the charge/discharge performance at high rate by using mesoporous lithium titanate as anode materials for lithium-ion batteries. In this study, mesoporous lithium titanate was synthesized via acidized carbon black as templates under hydrothermal condition. Carbon black templates could be easily removed after calcining the as-fabricated powder, creating mesoporous $Li_4Ti_5O_{12}$ structure.

2. Experimental

Mesoporous lithium titanate was synthesized by a simple hydrothermal method. In a typical synthesis, A stoichiometric amount of titanium isopropoxide and lithium acetate dihydrate (Li:Ti = 4:5) were mixed in 10 mL of ethanol solvent and stirred at room temperature. Carbon black was acidized by appropriate amount of sulfuric acid and hydrogen peroxide. The acidized carbon black was collected by centrifugation and cleaned by DI water repeatedly. Afterward, acidized carbon black was added in the precursor solution, transferring to a Teflon-lined stainless steel autoclave (45 mL in volume) and then reacting in an air-flow electric oven at 180 °C for 1 day. After cooling down naturally, the precipitate was harvested by centrifugation and washed thoroughly with ethanol for at least three times. The products were further dried for 1 day at 50 °C to obtain the Li–Ti–O precursor powder. The precursor powder was then calcined at 800 °C for 3 h to remove the inner acidized carbon black completely to obtain mesoporous lithium titanate. In order to compare the C-rate capability with different structure, non-porous lithium titanate was fabricated through the identical process without acidized lithium titanate additive.

The phase of as-synthesized powder was identified with an X-ray diffractometer (XRD, LabX XRD-6000, Shimadzu, Japan) operated at 30 kV and 20 mA using Cu Kα with a wavelength of 1.5406 Å. Morphological observation was carried out via field-emission scanning electron microscope (SEM; JSM-7600F, JEOL, Japan). The cross-section of mesoporous $Li_4Ti_5O_{12}$ powder was prepared by Ar ion milling with the cross-section polisher (CP, SM-09010, JEOL). The BET specific surface areas and average pore sizes were obtained from the N_2 adsorption/desorption isotherms at 77 K (Autosorb-1, Quantachrome). The BJH pore size distribution was determined from the desorption isotherms.

Electrochemical tests were performed by using two-electrode of 2032 type coin cells (20 mm in diameter and 3.2 mm thick). The cells contained an anode electrode, metallic lithium, polypropylene separator, and electrolyte of 1.0 M $LiPF_6$ in EC/DMC (1:2, vol.%), and were assembled in an argon glove box where both moisture and oxygen content were less than 1 ppm. The cells were cycled between 1 V and 2.5 V versus Li/Li+ at 0.5 C. The C-rate capability test was performed at the charge/discharge rate of 0.5, 1, 3, 5, 10, 20, and 30 C.

3. Results and discussion

3.1. Structure and morphology

Fig. 1 reveals the experimental flow of mesoporous $Li_4Ti_5O_{12}$. Initially, acidized carbon black was added during solvothermal process in the solution containing titanium isopropoxide and lithium acetate dihydrate. The acidized carbon black could be well dispersed in the solution, owing to its hydrophilic surface. Upon heating at 180 °C under hydrothermal condition, titanium isopropoxide and lithium acetate dihydrate would proceed hydrolysis and condensation, leading to the formation of hydroxyl Li–Ti–O
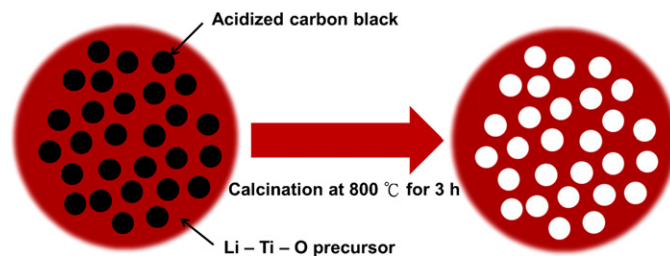

Fig. 1. The schematic plots of experimental flow chart in synthesizing mesoporous lithium titanate.

precursors. Accordingly, acidized carbon black was attracted in the hydroxyl Li–Ti–O precursors, due to the hydrogen bond interaction. Afterwards, Li–Ti–O precursors were calcined at 800 °C to obtain spinel $Li_4Ti_5O_{12}$ powder with good crystallinity. Meanwhile, inner carbon black as templates was also removed via calcination to generate mesoporous structure of lithium titanate. Herein, the porosity of mesoporous $Li_4Ti_5O_{12}$ could be well controlled by adjusting the amount of acidized carbon black. The current work aims to investigate the influence of mesoporous structure in the cycling performance in application of lithium-ion batteries. Thus, different porosity of mesoporous $Li_4Ti_5O_{12}$ would be discussed in the future.

X-ray diffraction patterns (XRD) of mesoporous structure and non-porous structure of $Li_4Ti_5O_{12}$ are shown in Fig. 2. All the sharp diffraction peaks can be indexed on the basis of a cubic spinel structure, $Li_4Ti_5O_{12}$ (JCPDS file no. 26-1198). This suggests that high purity $Li_4Ti_5O_{12}$ could be prepared by firing the Li–Ti–O precursors at 800 °C. Furthermore, no impurity was detected through X-ray diffraction pattern in both mesoporous and non-porous structure of lithium titanate. It was demonstrated that the incorporation of acidized carbon black did not result in the formation of impurity.

Fig. 3 shows the secondary electron images of mesoporous and non-porous structure of $Li_4Ti_5O_{12}$ anode materials. The diameter of mesoporous and non-porous $Li_4Ti_5O_{12}$ spheres were around 3 μm and 2 μm, respectively. The particle size of mesoporous lithium titanate was larger than that of non-porous lithium titanate. From the schematic flow chart in Fig. 1, acidized carbon black was introduced in the Li–Ti–O precursor. Upon calcination, acidized carbon black was reacted with oxygen to form CO_2 gas, leaving from lithium titanate. Thus, the particle size of mesoporous lithium titanate sphere was relatively large and the shape was also comparatively loose, as shown in Fig. 3a. Besides, the grain
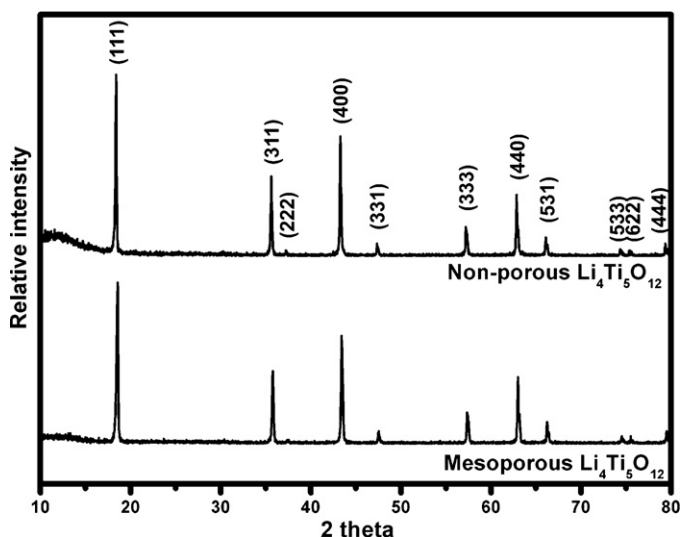

Fig. 2. The XRD patterns of mesoporous and non-porous lithium titanate.
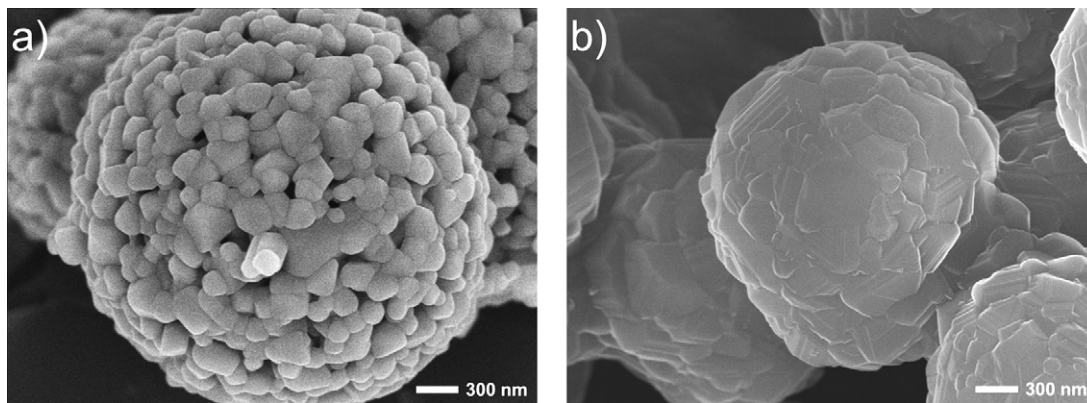
Fig. 3. The SEM images of (a) mesoporous and (b) non-porous lithium titanate spheres.

size of mesoporous lithium titanate was reduced via the addition of acidized carbon black. During calcination, the appearance of carbon black might interfere with the reaction from Li–Ti–O precursors to $Li_4Ti_5O_{12}$, further restraining lithium titanate from grain growth. On the other hand, the phenomenon of grain growth was rather severe in non-porous lithium titanate. The grain size of non-porous lithium titanate was larger than 300 nm, and the packing morphology of powder was dense. Consequently, the surface information could be investigated in detail by scanning electron microscopy. In fact, mesoporous structure might be obtained by incorporating templates. Tunneling electron microscopy technique was also a powerful method to analyze the structure and pore size distribution. Nevertheless, the particle size of $Li_4Ti_5O_{12}$ was too large to have incident electron beam to pass through, so the pore size distribution could not be realized via TEM image.

BEI images of cross-section view of mesoporous and non-porous structure of lithium titanate sphere is displayed in Fig. 4. Initially, the powder of lithium titanate was mounted by G2 glue. Next, the mounted sample was milled by Ar ion in the cross-section polisher. The pore size distribution was evaluated by the cross-section image of powder via scanning electron microscope. From the BEI image of mesoporous $Li_4Ti_5O_{12}$, the dark spots were related to pores, while the bright region was lithium titanate. It was revealed that the pores showed up not only on the surface of powder but also in the internal part of material. As a result, mixing acidized carbon black in the solution during hydrothermal process could generate mesoporous structure. On the other hand, the cross-section image of non-porous lithium titanate represented a smooth surface, as seen in Fig. 4b. There were completely no voids observed via BEI image of the

cross-section sample. Consequently, powders without templates additive during synthesis revealed the dense structure.

3.2. N_2 adsorption/desorption isotherms

From the SEM image of powder and the BEI image of cross-section sample in Figs. 3a and 4a, mesoporous structure could be spontaneously obtained by the support of templates additive. Nevertheless, the overall evidence of mesoporous architecture was also required. N_2 adsorption/desorption analysis was used to examine the mesoporous structure of lithium titanate, as shown in Fig. 5a. There is a hysteresis loop in the nitrogen adsorption–desorption isotherms of $Li_4Ti_5O_{12}$ with the aids of acidized carbon black, implying the filling of the mesoporous framework [18,19]. The mesoporous lithium titanate prepared in this study exhibits a type IV isotherm and a type H4 hysteresis loop, i.e. a typical mesoporous material. The Barrett–Joyner–Halenda (BJH) pore size distribution curve in Fig. 5b indicated that the mesoporous $Li_4Ti_5O_{12}$ materials exhibited a narrow pore size distribution, with average pore diameters around 4 nm, which was much smaller than the particle size of initial carbon black. Amorphous carbon would react with oxygen and produce CO_2, as the temperature was higher than 300 °C [9]. During calcination, the acidized carbon black was removed first. With increasing the temperature, the grain growth of lithium titanate occurred. Therefore, the pores remained in the internal of lithium titanate was shrunk by the grain coarsening. Furthermore, in comparison with non-porous lithium titanate, mesoporous structure of $Li_4Ti_5O_{12}$ revealed extra cavities, thus facilitating the lithium transportation during cycling.
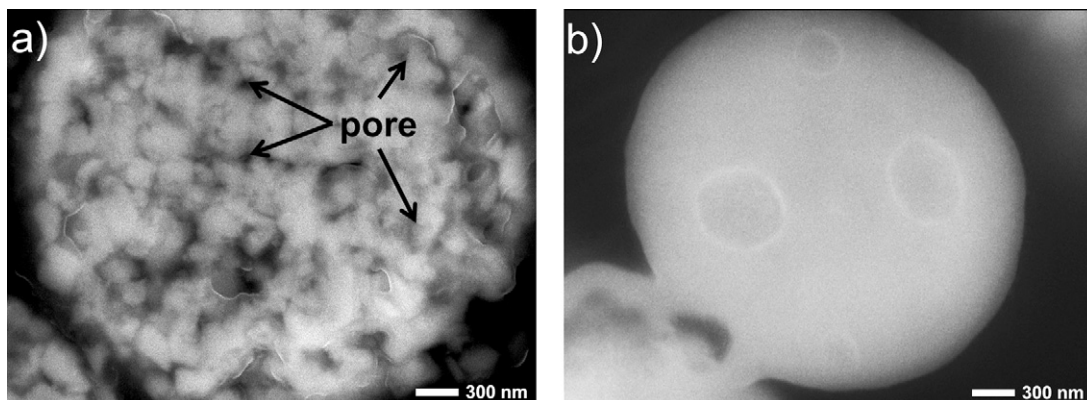

Fig. 4. The BEI images of cross-section samples derived from (a) mesoporous and (b) non-porous lithium titanate spheres.
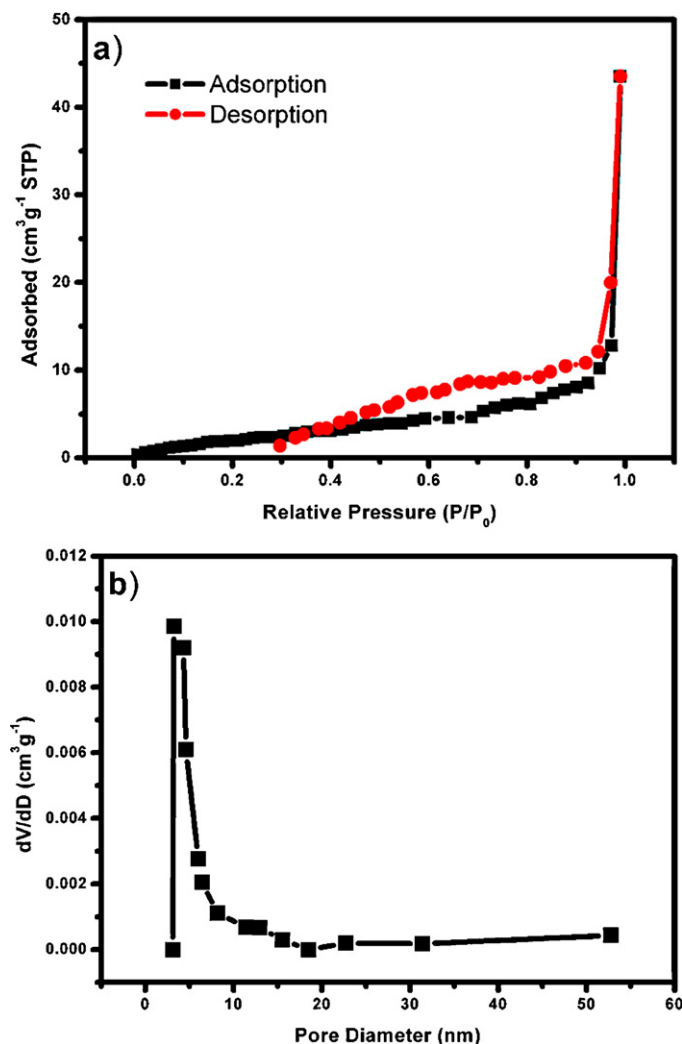
Fig. 5. (a) Nitrogen adsorption/desorption isotherms and (b) pore size distribution of mesoporous lithium titanate.

3.3. Cycling performance

Fig. 6 reveals the cycling stability of mesoporous and non-porous lithium titanate anode materials. The mesoporous lithium titanate exhibited a stable capacity of 140 mAhg^{-1} without severe fading at 0.5 C during 50 cycles, as shown in Fig. 6a. The initial capacity was around 140 mAhg^{-1}, and the 50th capacity was about 135 mAhg^{-1}. The total capacity fading was only 3.6% during 50 cycles. On the other hand, the non-porous Li$_4$Ti$_5$O$_{12}$ anode material displayed a rather poorer cycling performance at 0.5 C, as derived from Fig. 6b. The 1st capacity was around 115 mAhg^{-1}, and the 50th capacity decreased to near 100 mAhg^{-1}. Thus, the capacity decay increased to 13%, which was much larger than that of mesoporous structure. This might be attributed to the dense structure effect. From the SEM in Fig. 3b, the particle size of non-porous sphere was around 2 μm. During lithium insertion process, lithium ions migrated into material. The lithium transportation path was long, owing to the dense structure. Consequently, lithium ions did not react with lithium titanate completely, leaving unreacted region and further leading to relatively low capacity.

3.4. Rate capability

The C-rate capability of mesoporous and non-porous lithium titanate anode materials is shown in Fig. 7. The initial capacity of
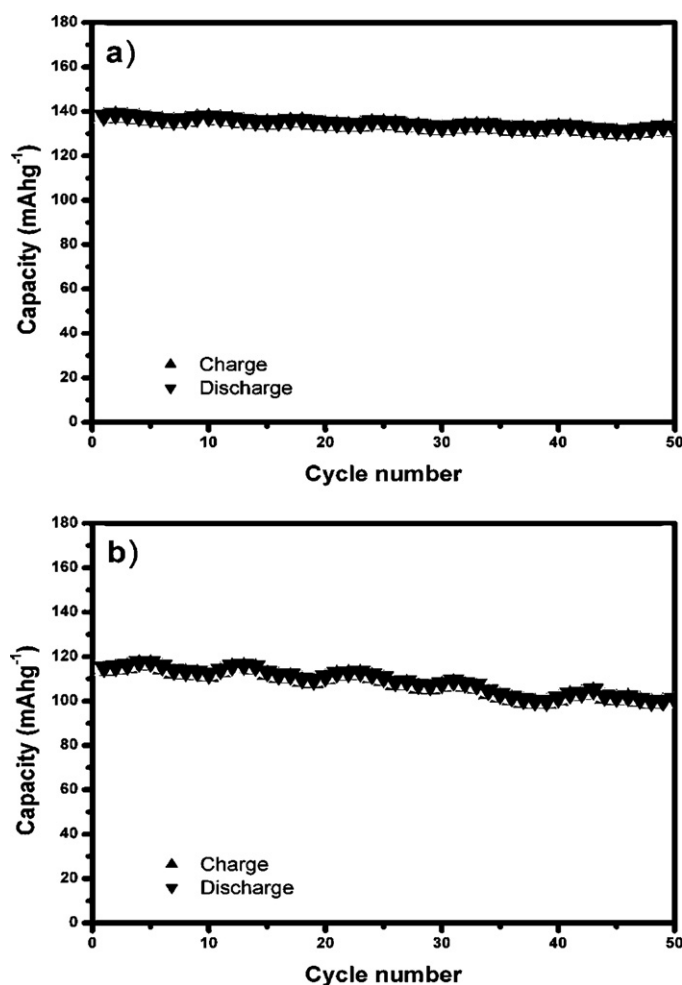

Fig. 6. The cycling stability at 0.5 C of (a) mesoporous and (b) non-porous lithium titanate spheres.

mesoporous lithium titanate at 0.5 C was around 140 mAhg^{-1}, as described in Fig. 7a. Afterward, the lithium insertion and extraction rates increased stepwise up to 30 C. The capacity of mesoporous lithium titanate at the current rate of 1, 3, 5, 10, 20, 30 C was around 132, 120, 115, 105, 83, 80 mAhg^{-1}, respectively. The mesoporous Li$_4$Ti$_5$O$_{12}$ anode material exhibits an outstanding performance at C-rate test. The reversible capacity of mesoporous lithium titanate at 5 C was as high as that of non-porous structure at 0.5 C, indicating that the rate capability could be significantly enhanced by architecture control. Additionally, the mesoporous lithium titanate at 30 C could still deliver a stable capacity of 80 mAhg^{-1}, reaching nearly 57% of capacity at 0.5 C. In other words, the charge process could be completed in 50 s, while still obtaining near half amount of theoretical capacity of lithium titanate. Remarkably, the capacity remained 140 mAhg^{-1}, as the current rate decreased to 0.5 C again. The excellent cycling stability at high C-rates was originated from the mesoporous structure. Accordingly, mesoporous structure could supply a short lithium transportation path, which was beneficial at high C-rate. As a result, the mesoporous structural development could be an efficient way to enhance the cycling stability. The C-rate performance of non-porous Li$_4$Ti$_5$O$_{12}$ is illustrated in Fig. 7b. As compared to the electrochemical property in mesoporous lithium titanate, the 1st charge capacity at 0.5 C was around 115 mAhg^{-1}. From the cycling performance with increasing C-rate, non-porous lithium titanate demonstrated a rather stable behavior. The capacity of non-porous lithium titanate at the current rate of 1, 3, 5, 10, 20, 30 C was around 100, 80, 70, 30, 23, 20 mAhg^{-1},
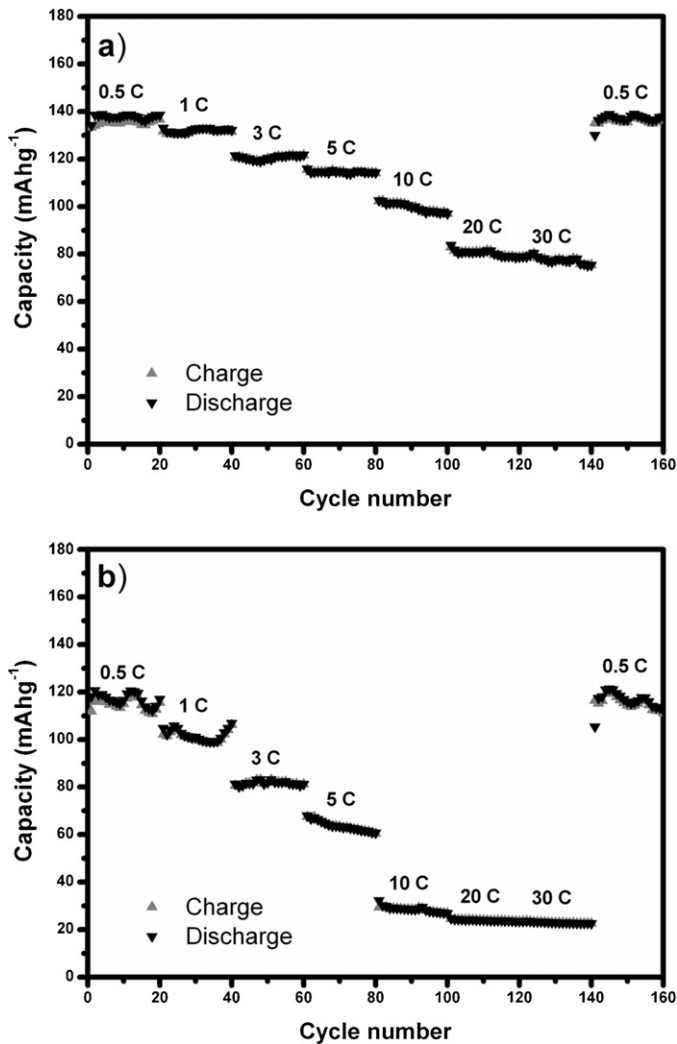
Fig. 7. The rate capability measurement of (a) mesoporous and (b) non-porous lithium titanate at various cycling rates of 0.5, 1, 3, 5, 10, 20, 30 C.
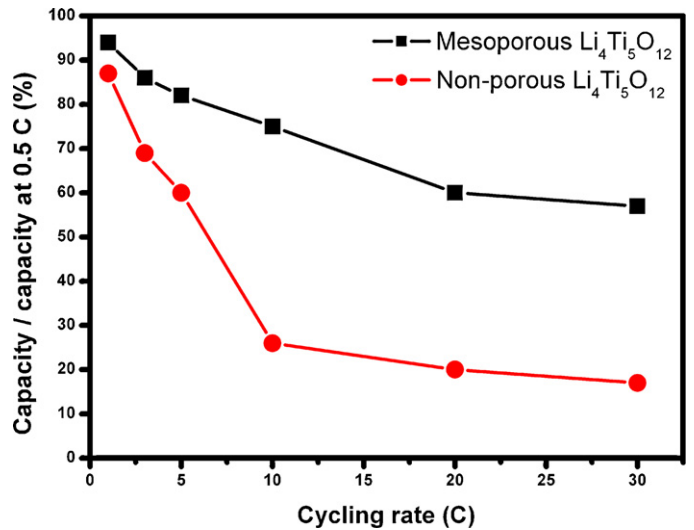

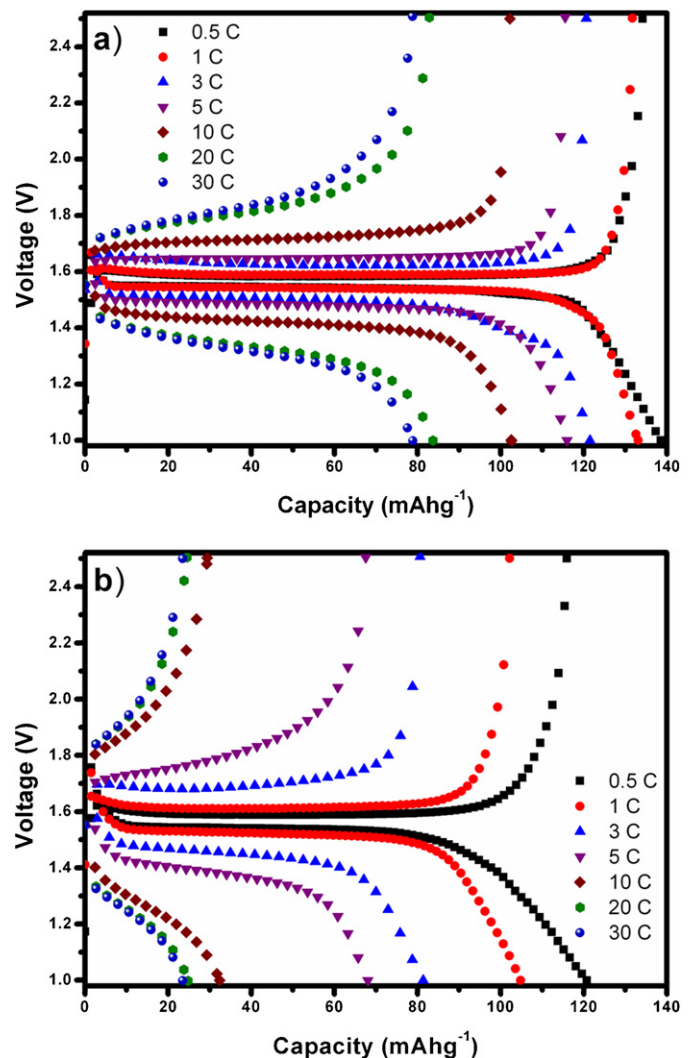Fig. 8. The ratio of capacity between several current rates and 0.5 C of mesoporous and non-porous lithium titanate.

Fig. 9. The voltage profiles of (a) mesoporous and (b) non-porous lithium titanate at various cycling rates of 0.5, 1, 3, 5, 10, 20, 30 C.

respectively. The capacity also reached 115 mAhg^{-1} as the charge rate was returned back to 0.5 C. It should be noted that the cycling stability under high current rates was significantly affected by the architectures. Herein, the mesoporous lithium titanate delivered a better cycling performance, owing to the shorter lithium diffusion route.

Fig. 8 describes the ratio of capacity between various current rates and 0.5 C. The rate capability was apparently improved by introducing mesoporous structure. The ratio of capacity remained higher than 80% with current rate of 5 C. Besides, the capacity at 30 C could deliver over 57% capacity at 0.5 C. Nevertheless, the capacity of non-porous $Li_4Ti_5O_{12}$ at 5 C was lower than 60% capacity at 0.5 C, even near to the capacity derived from mesoporous structure at 30 C. Besides, the ratio of capacity was rapidly dropped below 25%, as the current rate was higher than 10 C. It is apparent that the cycling stability at high rate was strongly related to the structure of lithium titanate.

In order to investigate the influence of structural variation in cycling behavior particularly, the voltage profiles of mesoporous and non-porous lithium titanate are illustrated in Fig. 9. All curves were selected during the first cycle under different current rates. It was demonstrated that the mesoporous material could sustain excellent charge and discharge rates. The voltage profiles of mesoporous $Li_4Ti_5O_{12}$ were nearly identical at 0.5 C and 1 C, as shown in
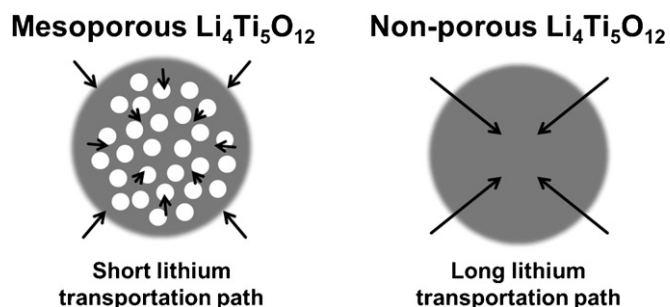
Fig. 10. The schematic plots during lithium intercalation/deintercalation in mesoporous and non-porous lithium titanate anode materials.

Fig. 9a. Then, the voltage decreased with increasing current density. It was 1.54 V at 0.5 C and dropped to 1.32 V at 30 C. Consequently, the polarization phenomenon with mesoporous structure was not severe for high rate cycling. On the other hand, it was revealed that non-porous $Li_4Ti_5O_{12}$ could not endure high cycling rates. Comparing to the discharge cycling behavior of mesoporous structure, the voltage of non-porous lithium titanate at 1 C was lower than that at 0.5 C, as displayed in Fig. 9b. In addition, the polarization extent was significant in non-porous structure. The voltage was 1.54 V at 0.5 C and then decreased to near 1.2 V at 30 C. Furthermore, the voltage plateaus nearly disappeared at above 10 C. In other words, the cell of non-porous lithium titanate failed to deliver a stable lithium intercalation/deintercalation behavior, as the current rate was higher than 10 C.

3.5. Mechanism

Fig. 10 reveals the schematic plots of lithium transportation path in mesoporous and non-porous structures. In the lithium insertion and removal process, mesoporous structure could shorten the lithium transportation distance, owing to the uniform pore distribution. In contrast, the lithium transportation routes of non-porous structure were rather longer than that in mesoporous material. Lithium ions were required to diffuse leisurely into lithium titanate sphere. Eventually, lithium intercalation/deintercalation reactions in the center of lithium titanate were not occurred. Non-porous structure could not sustain stable capacity at high charge/discharge rates. However, with the mesoporous structure, lithium ions could be migrated into the materials completely at the same time even at high cycling rates. As a result, mesoporous structure could exhibit an excellent cycling stability, especially at high C-rate.

4. Conclusion

Mesoporous structure of lithium titanate was successfully fabricated with the incorporation of acidized carbon black during hydrothermal process and then calcinations. A formation mechanism was proposed to account for the production of mesoporous spheres. Mesoporous structure was well demonstrated through SEM images of powder, BEI images of cross-section samples and N_2 adsorption/desorption isotherm. The mesoporous lithium titanate manifests a superior cycling performance. The capacity was 80 mAhg^{-1} at 30 C, displaying over 57% of capacity at 0.5 C. Mesoporous structure creates a rapid lithium transportation path and facilitates the C-rate capability. As a result, the mesoporous lithium titanate might be a promising anode material as high-performance anodes for next-generation LIBs.

References

[1] H. Zheng, K. Jiang, T. Abe, Z. Ogumi, Carbon 44 (2006) 203–210.
[2] M. Winter, J.O. Besenhard, Electrochim. Acta 45 (1999) 31–50.
[3] Y.S. Lin, J.G. Duh, D.T. Shieh, M.H. Yang, J. Alloys Compd. 490 (2010) 393–398.
[4] W.R. Liu, J.H. Wang, H.C. Wu, D.T. Shieh, M.H. Yang, N.L. Wu, J. Electrochem. Soc. 152 (2005) A1719–A1725.
[5] T. Ohzuku, A. Ueda, N. Yamamoto, J. Electrochem. Soc. 142 (1995) 1431–1435.
[6] H. Ge, N. Li, D. Li, C. Dai, D. Wang, J. Phys. Chem. C 113 (2009) 6324–6326.
[7] C.T. Hsieh, J.Y. Lin, J. Alloys Compd. 506 (2010) 231–236.
[8] P.P. Prosini, R. Mancini, L. Petrucci, V. Contini, P. Villano, Solid State Ionics 144 (2001) 185–192.
[9] Y.S. Lin, J.G. Duh, M.H. Hung, J. Phys. Chem. C 114 (2010) 13136–13141.
[10] Y.S. Lin, J.G. Duh, H.S. Sheu, J. Alloys Compd. 509 (2011) 123–127.
[11] Y. Tang, L. Yang, Z. Qiu, J. Huang, J. Mater. Chem. 19 (2009) 5980–5984.
[12] L. Shen, C. Yuan, H. Luo, X. Zhang, K. Xu, Y. Xia, J. Mater. Chem. 20 (2010) 6998–7004.
[13] E.M. Sorensen, S.J. Barry, H.K. Jung, J.R. Rondinelli, J.T. Vaughey, K.R. Poeppelmeier, Chem. Mater. 18 (2006) 482–489.
[14] S.W. Woo, K. Dokko, K. Kanamura, Electrochim. Acta 53 (2007) 79–82.
[15] Y. Tang, L. Yang, S. Fang, Z. Qiu, Electrochim. Acta 54 (2009) 6244–6249.
[16] N. He, B. Wang, J. Huang, J. Solid State Electrochem. 14 (2010) 1241–1246.
[17] C. Jiang, Y. Zhou, I. Honma, T. Kudo, H. Zhou, J. Power Sources 166 (2007) 514–518.
[18] Y.F. Lee, K.H. Chang, C.C. Hu, K.M. Lin, J. Mater. Chem. 20 (2010) 5682–5688.
[19] K.S.W. Sing, Pure Appl. Chem. 54 (1982) 2201–2218.